Concentrated Electrolytes Enabling Stable Aqueous Ammonium-Ion Batteries

Jin Han, Maider Zarrabeitia, Alessandro Mariani, Matthias Kuenzel, Angelo Mullaliu, Alberto Varzi,* and Stefano Passerini*

Rechargeable aqueous batteries are promising devices for large-scale energy-storage applications because of their low-cost, inherent safety, and environmental friendliness. Among them, aqueous ammonium-ion (NH_4^+) batteries (AAIB) are currently emerging owing to the fast diffusion kinetics of NH_4^+. Nevertheless, it is still a challenge to obtain stable AAIB with relatively high output potential, considering the instability of many electrode materials in an aqueous environment. Herein, a cell based on a concentrated (5.8 M) aqueous $(NH_4)_2SO_4$ electrolyte, ammonium copper hexacyanoferrate (N-CuHCF) as the positive electrode (cathode), and 3,4,9,10-perylene-bis(dicarboximide) (PTCDI) as the negative electrode (anode) is reported. The solvation structure, electrochemical properties, as well as the electrode–electrolyte interface and interphase are systematically investigated by the combination of theoretical and experimental methods. The results indicate a remarkable cycling performance of the low-cost rocking-chair AAIB, which offers a capacity retention of ≈72% after 1000 cycles and an average output potential of ≈1.0 V.

1. Introduction

The exploitation of renewable energy sources, that is, solar, wind, hydro, tidal, and geothermal, is becoming essential to reduce air pollution and global warming caused by the combustion of traditional fossil fuels.[1,2] Given their intermittent nature, effective energy storage systems (ESSs) are needed to store the produced electricity.[3] Among the available ESSs, batteries appear attractive because of their modularity and

J. Han, M. Zarrabeitia, A. Mariani, M. Kuenzel, A. Mullaliu, A. Varzi, S. Passerini
Helmholtz Institute Ulm (HIU)
Helmholtzstrasse 11, D-89081 Ulm, Germany
J. Han, M. Zarrabeitia, A. Mariani, M. Kuenzel, A. Mullaliu, A. Varzi, S. Passerini
Karlsruhe Institute of Technology (KIT)
P.O. Box 3640, D-76021 Karlsruhe, Germany
E-mail: alberto.varzi@kit.edu; stefano.passerini@kit.edu

adaptability for homes, communities, and the grid.[4,5] Although non-aqueous lithium-ion batteries (LIBs) are the technology of choice for electromobility, cost and safety issues caused by the flammable and volatile organic electrolyte hinder their wide application in large-scale stationary applications,[6] in which cost and safety are the determining factors instead of energy density.[7] In this context, rechargeable aqueous batteries, which use non-flammable and less-volatile aqueous electrolytes become appealing alternatives for large-scale stationary applications.[8,9]

The first aqueous battery based on $LiMn_2O_4//VO_2$, featuring a "rocking-chair" mechanism was proposed by Dahn's and co-workers in 1994.[10] The limited electrochemical window of aqueous electrolytes was extended in 2015 by using a "water-in-salt" electrolyte designed by Wang's group, demonstrating a $LiMn_2O_4//Mo_6S_8$ aqueous LIB with a high output potential of 2.3 V.[11] Beyond aqueous LIBs, other aqueous chemistries based on alternative metallic cations, that is, Na+,[12–14] K+,[15,16] Zn2+,[17–19] Mg2+,[20,21] Ca2+[22] and Al3+,[23] are currently being intensively investigated. Alongside, aqueous ammonium-ion batteries (AAIBs) using non-metallic NH_4^+ are gradually emerging, driven by the NH_4^+ fast diffusion kinetics.[24,25] Indeed, NH_4^+ possesses a small hydrated ionic radius (3.31 Å) providing fast diffusion kinetics.[26] Despite some pioneering works[24,27] have demonstrated the potential of this battery chemistry, it is still very challenging to develop a stable full "rocking-chair" AAIB with high coulombic efficiency, due to the instability of electrode materials in the present diluted aqueous electrolytes.

To address the above-mentioned challenge, two main strategies can be adopted. The first is to develop novel and stable electrode materials. Among the so far proposed electrode materials, the cost-efficient Prussian blue and its analogues (PBA), owing an open framework and large interstitial sites, have been intensively researched.[28–30] In addition, several inorganic materials including Ti_3C_2 MXenes,[27] V_2O_5,[31] $TiO_{1.85}(OH)_{0.30} \cdot 0.28H_2O$,[32] $Fe_5V_{15}O_{39}(OH)_9 \cdot 9H_2O$,[33] MoO_3,[34] VS_2/VO_x,[35] $NH_4V_4O_{10}$,[36] MnO_x,[37,38] as well as organic compounds such as 3,4,9,10-perylene tetracarboxylic diimide (PTCDI),[24] 1,4,5,8-naphthalene tetracarboxylic dianhydride-derived polyimide (PNTCDA),[39] polyaniline[40] and covalent organic frameworks (COFs)[41] have been investigated.

ADVANCED
SCIENCE NEWS
www.advancedsciencenews.com

ADVANCED
MATERIALS
www.advmat.de

The second approach consists in tuning the electrolyte composition. With regards to the electrolyte composition, concentrated aqueous electrolytes and functional additives based on "common ion effect" have been employed by Ji's group and Shu's group, respectively, to improve cycling stability of AAIBs.[39,42]

Inspired by these two complementary strategies, herein, a stable Cu-based PBA cathode (N-CuHCF) and PTCDI anode are selected as electrode materials. More importantly, diluted (1 M) and concentrated (5.8 M) aqueous $(NH_4)_2SO_4$ electrolytes, respectively denoted as LCE and HCE, are comparatively characterized. The solvation structure, electrochemical properties, electrode–electrolyte interphase, and performance in a full cell are systematically investigated and discussed.

2. Results and Discussion

Classic molecular dynamics (MD) simulations were performed to clarify the molecular interactions in LCE and HCE. A snapshot of a randomly selected frame of the LCE (I) and HCE (II) electrolytes are displayed in **Figure 1**a, depicting a 10 Å thick slice of the box (only the ions are reported for sake of clarity). Other than the obvious different number of ions, the

establishment of ion-rich domains is observed, especially for the HCE system. The spatial distribution functions (SDFs) for H_2O, NH_4^+, and SO_4^{2-} are shown for the 1 M (Figure 1b-I,b-III,b-V) and HCE (Figures 1b-II,b-IV,b-VI) electrolytes. It is noted that the surfaces are plotted for an isovalue of twice the average bulk density. Albeit the relative approaching distances of the solvating molecules with respect to the central molecule stays the same in both electrolytes, the amount of coordinating species changes according to the salt concentration. For example, in HCE there are more NH_4^+ cations interacting with water (compare Figures 1b-I,b-II) and SO_4^{2-} anions interacting with NH_4^+ (compare Figures 1b-III,b-IV), while less water molecules interact with the NH_4^+ cation.

Radial distribution functions (RDFs) are also employed to analyze the solvation shells of the species. As shown in Figure 1c, the hydrogen bonding network is precisely investigated by looking at the RDFs of hydrogen bonded pairs. In both electrolytes, the hydrogen bond length increases in the order anion–water (1.75 Å) < water–water (1.82 Å) < ion pair (1.85–1.88 Å) < cation–water (1.95 Å). The only interaction for which the correlation length is shifting with the concentration is the ion pair one, becoming slightly weaker (i.e., ions are moving further apart) as a possible result of the increased
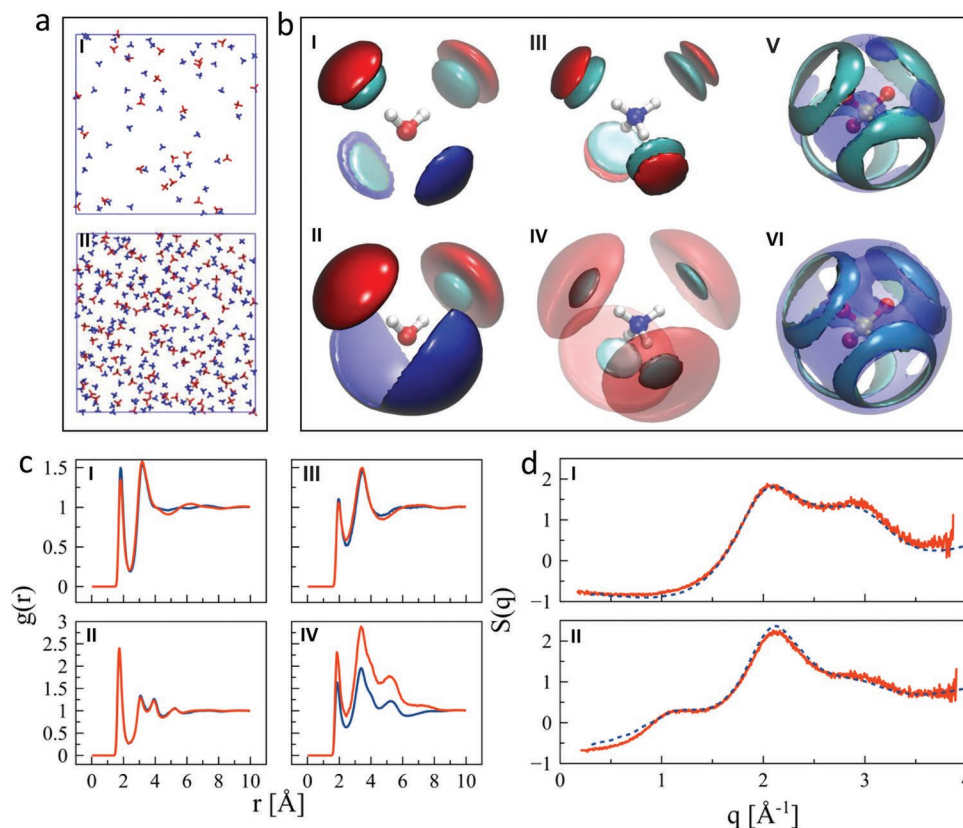

Figure 1. a) Randomly selected 10 Å thick slices from the simulation of LCE (a-I) and HCE (a-II). In both panels, ammonium cations and sulfate anions are represented in blue and red, respectively. Water molecules are not shown for clarity. b) Spatial distribution functions (SDFs) for H_2O (cyan), NH_4^+ (blue), and SO_4^{2-} (red) illustrated in LCE (b-I,b-III,b-V) and HCE (b-II,b-IV,b-VI). The surfaces are plotted for an isovalue of twice the average density. c) Selected radial distribution functions for H_2O–H_2O (c-I), H_2O–NH_4^+ (c-III), H_2O–SO_4^{2-} (c-II), and the NH_4^+–SO_4^{2-} ion pairs (c-IV). In all four panels, LCE and HCE are displayed in blue and red, respectively. d) Experimental small- and wide-angle X-ray scattering (SWAXS) patterns and the corresponding patterns extracted from the simulations for LCE (d-I) and HCE (d-II) electrolytes. In both panels, the experimental patterns are displayed in red solid line and the calculated patterns are displayed in blue dotted line.

emerging dielectric constant of the medium, effectively screening the Coulombic forces. A more insightful result is obtained by checking the coordination numbers of each species, as reported in Table S1, Supporting Information. It is immediately clear how the amount of "free" water (intended as water molecules only bound to other water molecules) is drastically diminished. The solvation shell of water changes from 8.8:1 (water:ions) to an almost equimolar 1.26:1 ratio. As a direct consequence of the increased concentration, the hydration shell of both ions is depleted, while ion-pairing is enhanced.

Finally, the experimental small- and wide-angle X-ray scattering (SWAXS) patterns of the two electrolytes were collected and compared with those extracted from the simulations (see Figure 1d). The agreement between experiment and theory is excellent, thus it is possible to confidently state that the models accurately represent the structure of the real systems. For both concentrations, the typical double peak between 2 and 3 Å^{-1} characteristic of water is observed, but it appears to be vastly distorted in the HCE, hinting at a profoundly modified water solvation shell, as discussed above. More interestingly, though, an emerging new peak at $q \approx 1\text{Å}^{-1}$ is discovered in the HCE. Such a feature should not be interpreted as the "pre-peak" found in some ionic liquids (ILs),[43,44] because the pre-peak of ILs is found at much smaller q values. The new peak for HCE is instead ascribable to the charge–charge correlation,[45] that is, the repeating distance between two homologue ions (cations or anions) mediated by an oppositely charged ion (anions or cations), as schematized in Figure S1a, Supporting Information. Such repeating correlation eventually leads to the formation of ion channels, as shown in Figure S1b, Supporting Information.

Additional physical-chemical properties of the electrolytes, that is, shelf-life stability, thermal stability, pH value, and ionic conductivity were also evaluated. The photographs of HCE solutions after preparation (Figure S2a, Supporting Information) and storage for 2 weeks (Figure S2b, Supporting Information) show no sign of salt precipitation, indicating a good shelf-life stability. The vertically offset differential scanning calorimetry (DSC) of LCE (Figure S3a, Supporting Information) and HCE (Figure S3b, Supporting Information) show a substantial decrease of the crystallization temperature from ca. −19.3 °C for LCE to −46.5 °C for HCE. Moreover, pH values of the two electrolytes are reported in Table S2, Supporting Information. HCE shows slightly lower pH value (5.35) compared to LCE (5.82). In addition, the ionic conductivities of $(NH_4)_2SO_4$ solutions with different salt concentration were determined (Table S3, Supporting Information). The ionic conductivity continuously increases when the concentration is raised from 1 to 4 m, while it only slightly decreases from 4 to 5.8 m. Nevertheless, the 5.8 m electrolyte still displays a rather high ionic conductivity and an outstanding electrochemical stability (see later), motivating the choice of this composition for the study.

The electrochemical stability window (ESW) of LCE and HCE was first evaluated by linear sweep voltammetry (LSV) using a Ti foil working electrode as displayed in **Figure 2**a. In conventional LCE, the cathodic decomposition begins at around −0.76 V (versus Ag/AgCl), while in the anodic direction the current start rising at ≈0.58 V (versus Ag/AgCl), thus resulting in an ESW of just 1.34 V. In contrast, the more concentrated electrolyte shows current increase when the potential exceeds −1.03

and 1.34 V (versus Ag/AgCl) in the cathodic and anodic scan, respectively. The ESW is broadened to 2.39 V, that is, more than 1 V is gained compared to the diluted solution. In the enlarged plots for both the cathodic and anodic side, two obvious shoulders are evident in HCE. This may be related to the formation of surface layers, which will be discussed later.

CV measurements of N-CuHCF positive (cathode) electrodes were performed using either LCE or HCE in the working potential range from 0.4 to 1.05 V (versus Ag/AgCl) with three-electrode cells (see in Figure 2b). As seen from these CV curves, the reversibility and cycling stability of N-CuHCF is substantially enhanced by the use of HCE. Interestingly, the characteristic redox peaks also shift to a higher potential (0.835/0.878 V) compared to those recorded in LCE (0.790/0.846 V). This may be due to the enhanced ion-pairing caused by the depleted hydration of both ions.[46] Additionally, the peak separation in HCE is substantially reduced (just 0.043 V versus 0.056 V in LCE).

The CV curves at different scan rates (0.1, 0.2, 0.4, 0.8, 1, 2, 4, 6, and 8 mV s^{-1}) for N-CuHCF electrodes in either LCE or HCE are also presented in Figures 2c,2d, respectively. A substantial peak shift (and increase in peak separation) is found as the sweep rate increases, but the redox processes appear still reversible. Notably, the current remains low even when approaching the limit of ESW, indicating the outstanding stability of the HCE. Differently, the current in the 1 m electrolyte increases, especially at high scan rates, ≈1.05 V (versus Ag/AgCl), possibly as a result of O_2 evolution, which is in agreement with the data reported in Figure 2a. Additionally, the corresponding log(i) versus log(v) plots, which present the logarithm of peak current density at a given scan rate as a function of the logarithm of the scan rate, in LCE and HCE are displayed for both the cathodic and the anodic peaks (see Figure S4, Supporting Information). Assuming that the current peak obeys a power-law relationship with the sweep rate:

$$i = av^b \tag{1}$$

where a and b are fitting parameters,[47] by plotting log(i) against log(v) the b-value can be extracted from the slope. Generally, a b-value of 0.5 indicates a diffusion-controlled process, while a b-value of 1 reveals a surface-controlled process.[48] After the plotting and fitting, b-values of 0.6 result for both cathodic and anodic currents using LCE, supporting for a mostly diffusion-controlled process. Differently, b-values closer to one are obtained for the cathodic and anodic peaks (more precisely 0.93 and 0.92, respectively) recorded using HCE, which indicates a less diffusion-limited process for HCE compared to LCE in the provided sweep rate range from 0.1–8 mV s^{-1}. The selected CV curves at different scan rates (0.1 and 0.2 mV s^{-1}) for N-CuHCF electrodes (shown in Figure S6, Supporting Information) display similar shape in both LCE and HCE. The similar CV area (especially at low scan rate) recorded using the two electrolytes (LCE and HCE) suggests that the amount of NH_4^+ stored by N-CuHCF is practically independent from the salt concentration in the electrolyte. CV measurements of PTCDI-based electrodes in either LCE or HCE were carried out in the working potential range from −1.0 to 0.3 V (versus Ag/AgCl) (see in Figure 2e). As it was the case for the N-CuHCF cathode, the reversibility and cycling stability of PTCDI is enhanced when
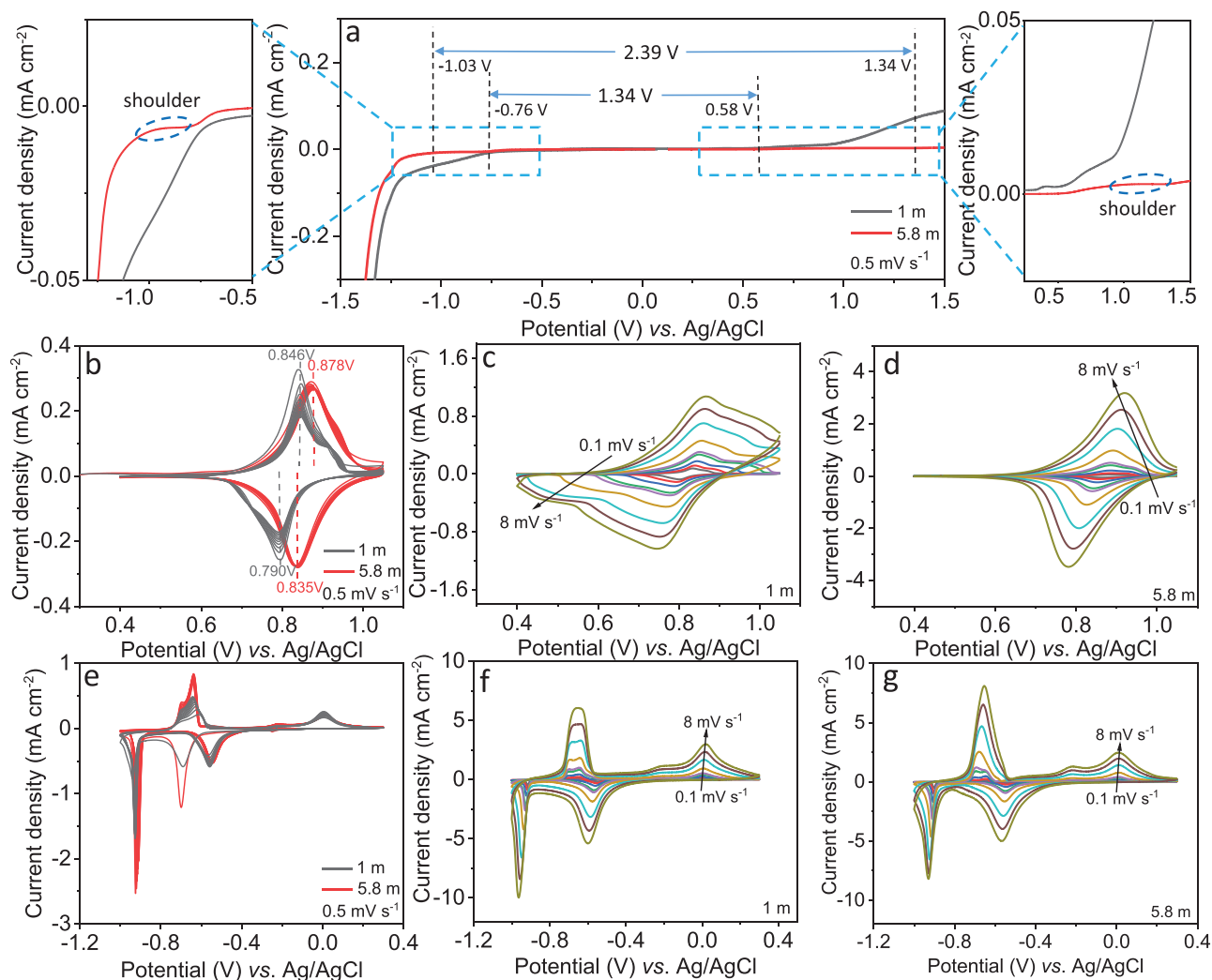
Figure 2. a) Electrochemical stability window of the LCE and HCE determined by linear sweep voltammetry (LSV). The anodic and cathodic sweeps are each performed on fresh cells. b) Initial 10 cyclic voltammetry (CV) curves of N-CuHCF electrode coated on Ti foil employing LCE and HCE. c,d) CV curves at different scan rates for N-CuHCF electrodes in LCE (c) and HCE (d) electrolytes. e) Initial 10 cyclic voltammetry (CV) curves of PTCDI electrodes coated on Ti foil employing LCE and HCE. f,g) CV curves at different scan rates of PTCDI electrodes in LCE (f) and HCE (g) electrolytes.

the salt concentration in the electrolyte is increased from 1 to 5.8 м. The CV measurements at different scan rates for PTCDI electrodes in either LCE or HCE were also performed (see Figures 2f,g) and the corresponding $\log(i)$ against $\log(v)$ plots are provided in Figure S5, Supporting Information. For the analysis, the redox peaks at −0.59/0.02 V are chosen considering that the reduction peak at around −0.9 V is too close to the H_2 evolution potential. Once more, the b-values obtained by fitting are rather close to 1 for HCE, indicating that the process is less diffusion-limited. Selected CV curves at different scan rates (0.1 and 0.2 mV s^{-1}) for PTCDI electrodes are reported in Figure S7, Supporting Information. Once again, the highly comparable curves confirm that the amount of NH_4^+ hosted by PTCDI is similar in LCE and HCE.

In order to understand whether an SEI-type layer is formed on electrodes in LCE and HCE, the surface chemical composition of polarized electrodes was studied via XPS. The measurements were performed employing bare Ti foil electrodes

after exposure to the electrolytes for 6 h (at OCV), and linearly sweeping the potential to 1.2 and −0.9 V in anodic and cathodic direction, respectively. The O 1s, N 1s, and S 2p XP spectra of such electrodes tested in LCE and HCE are displayed in **Figure 3**a and 3b, respectively. For reference, the XPS spectra of the pristine Ti current collector are reported in Figure S8, Supporting Information. The surface of pristine Ti foil is mainly composed of TiO_2 and, in a lower amount, by other oxides, that is, Ti_2O_3, TiO, and carbonates, such as $CaCO_3$,[49,50] as well as TiN. The latter species is highly reactive to oxygen leading to oxide overlayers.[51]

Once the Ti foils are placed in contact with the electrolyte, but not polarized (i.e., at OCV), the surface is covered by the electrolyte salt, as shown by the O 1s spectra (Figure 3a,b) where a slight decrease of the TiO_2 peak is observed. This is further supported by the presence of an extra peak related to $(NH_4)_2SO_4$ salt such as −S=O at 532.5 eV and NH^{4+} at 402 eV in N 1s (Figure 3a,b).[49] The surface composition of the Ti

ADVANCED
SCIENCE NEWS
www.advancedsciencenews.com

ADVANCED
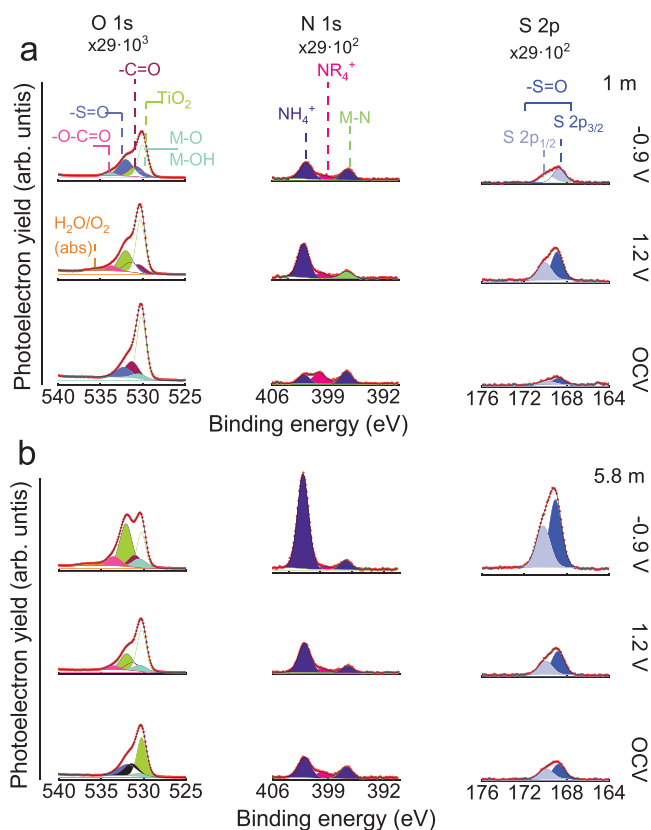**MATERIALS**
www.advmat.de

Figure 3. a,b) XPS spectra of Ti current collectors collected at OCV, and after sweeps to 1.2 and −0.9 V during the LSV sweep process in LCE (a) and HCE (b) electrolytes.

current collector polarized up to 1.2 V or down to −0.9 V is similar in both the electrolytes. In fact, the observed species mainly correspond to the electrolyte salt, as observed at OCV (−S=O and NH^{4+}) suggesting that the salt is not decomposed. However, two differences can be found. On the one hand, the O 1s (Figure 3a) shows a small peak toward higher binding energies (≈535.5 eV) when LCE was employed. This peak corresponds to chemically absorbed oxygen, which might be formed due to the O_2 evolution expected to occur in LCE (see Figure 2a).[52] This is in agreement with the slightly higher sulfuric atomic concentration (see Figure S9, Supporting Information), likely because $(NH_4)_2SO_4$ precipitates on the Ti foil as a result of water decomposition. In fact, the Ti surface in HCE is covered by a substantial amount of electrolyte salt (see O 1s, N 1s, and S 2p in Figure 3b). In summary, a surface layer is certainly present on the electrode, as demonstrated by XPS results. However, this is likely the result of salt precipitation rather than an SEI-like layer formed by reductive decomposition of the cation and/or the anion.

To verify the concentration of K, Na, Fe, and Cu and water amount in the CuHCF precursor and the ion-exchanged N-CuHCF cathode, inductively coupled plasma optical-emission spectrometry (ICP-OES) (see Table S4, Supporting Information) and thermogravimetric analysis (TGA) (see Figure S10, Supporting Information) have been conducted. Additionally, the 1st charge capacity of N-CuHCF has been used to verify the amount

of NH_4^+. As a result, the formulae of N-CuHCF and CuHCF are determined to be $(NH_4)_{0.76}Cu[Fe(CN)_6]_{0.67} \cdot \square_{0.33} \cdot 3.55H_2O$ and $K_{0.38}Na_{0.05}Cu[Fe(CN)_6]_{0.67} \cdot \square_{0.33} \cdot 2.63H_2O$, respectively. The deviation from the Fe/Cu = 1/1 stoichiometry reveals lattice defects in the form of $[Fe(CN)_6]^{4-}$ vacancies, which is labelled as $\square$ in the formulas. Indeed, a low amount of sodium and potassium are revealed in N-CuHCF by ICP-OES in Table S4, Supporting Information, which indicates the successful ion-exchange strategy. XRD patterns of CuHCF (see Figure S11, Supporting Information) and N-CuHCF powders (**Figure 4**a) were also collected, and the corresponding Rietveld refinements were carried out. The results show that both samples feature a cubic structure (s.g.: $Fm\overline{3}m$, 225) with lattice parameter: $a = 10.05229(25)$ Å; $V = 1015.77(8)$ Å^3 for CuHCF and $a = 10.0377(5)$ Å; $V = 1011.36(14)$ Å^3 for N-CuHCF. The atomic positions, occupancy, and isotropic atomic displacement parameter are summarized in Table S5, Supporting Information. NH_4^+ is most likely accommodated in the $8c$ Wyckoff sites in N-CuHCF, replacing the alkali metal cations in CuHCF. Given the high structural similarity ($\Delta a \approx 0.1\%$), we can assume that the insertion of NH_4^+ does not induce any significant lattice strain.

To investigate the structural and electronic evolution of N-CuHCF upon cycling, ex situ X-ray absorption near-edge spectroscopy (XANES) and XRD measurements have been conducted at different states of charge. Besides the N-CuHCF powder (P0), three ex situ samples were prepared, that is, pristine (E1), charged (E2) and discharged (E3) electrodes, as shown in Figure 4b. XANES spectra reveal the evolution in electronic features for both Cu and Fe. The normalized XANES spectra at the Cu K-edge and Fe K-edge for the powder and all ex situ samples are presented in Figures 4c,f, respectively. The pre-edge region stems from 1s → bound states transitions, revealing important electronic features such as oxidation state and spin configuration. Thus, a pre-edge region analysis was carried out (see Supporting Information) and the parameters retrieved from the Cu pre-edge fitting analysis are shown in Table S6, Supporting Information. The Cu pre-edge region was fitted with three main contributions: in particular, the transition occurring at ≈8981–8982 eV is commonly attributed to the Cu(I) 1s → 4p transition and is, therefore, a signature of Cu(I).[53,54] By taking a closer look at this region in samples P0 and E1 (see Figure 4d), E1 displays a clear transition at ≈8981 eV, pointing out the presence of monovalent copper. On the contrary, P0 is mainly constituted by Cu(II). For this reason, we assume a partial reduction process of Cu(II) into Cu(I) during the slurry preparation, as described in the Experimental Section. At the same time, the lattice parameter a in the E1 sample contracts is supposedly due to the partial Cu^{II}/Cu^{I} reduction. In Figure 4e, the pre-edge region of E2 has no detectable transition at ≈8982 eV, in agreement with the oxidation of Cu(I) to Cu(II) during the first charge. As proven by Rietveld refinement, the ion extraction process and simultaneous metals' oxidation determine an expansion of the lattice (Figure S12, Supporting Information). In the subsequent discharge, Cu is not actively involved in the electrochemical reaction, as evidenced by the spectral shape of E3. Only a very low-intensity transition is detected in the pre-edge region of E3 (see Figure 4e and "Peak B" in Figure S13, Supporting Information), which might be
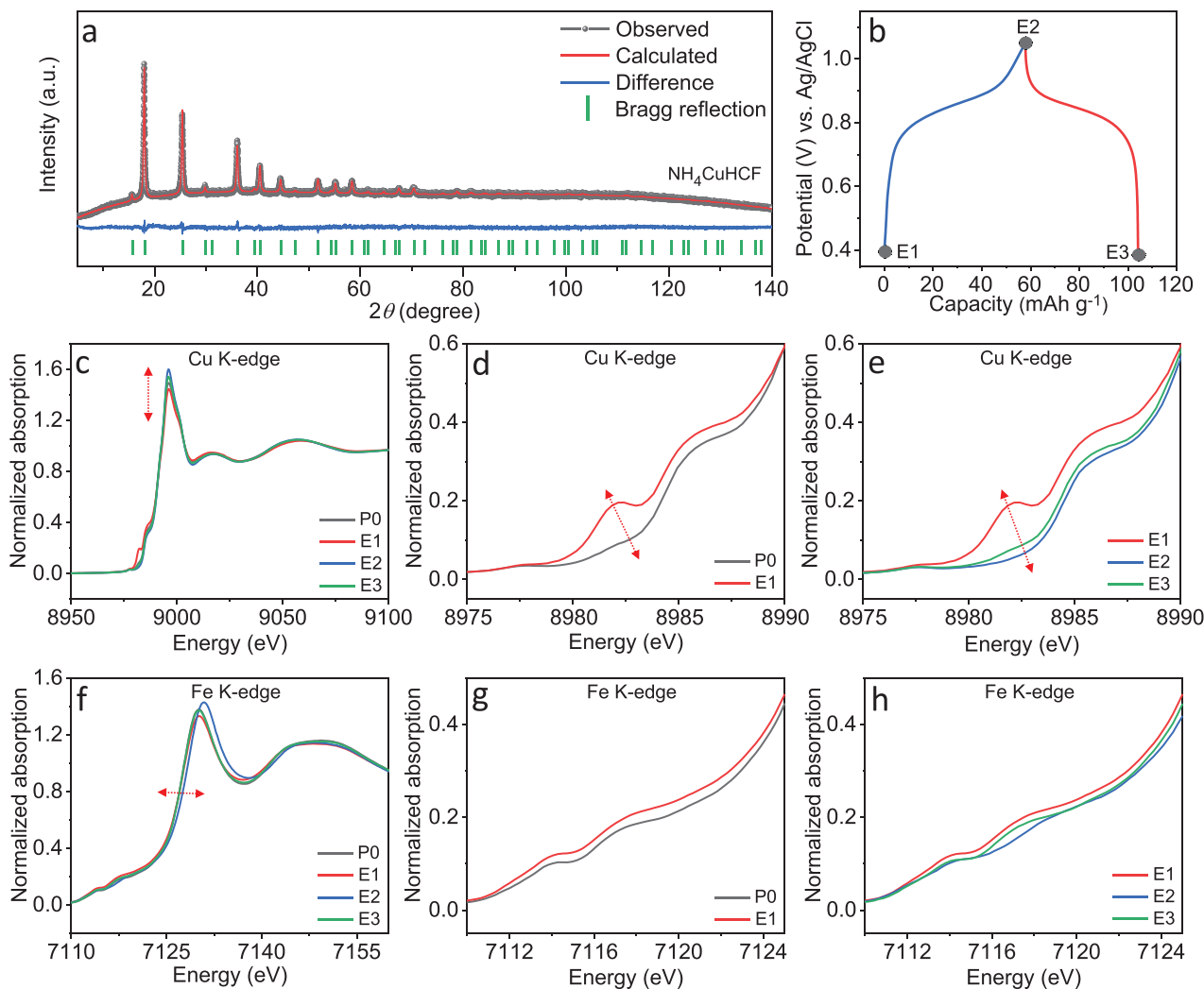
Figure 4. a) Rietveld refinements of N-CuHCF powders XRD pattern. b) Typical charge–discharge potential profiles of the N-CuHCF electrodes for the first cycle in a 3-electrode Swagelok cell. The highlighted points correspond to the states of charge selected for the ex situ XANES measurements. c) Normalized Cu K-edge of the N-CuHCF pristine powder (P0), the pristine N-CuHCF electrode (E1), fully charged N-CuHCF electrode (E2), and fully discharged N-CuHCF electrode (E3). d,e) Enlarged plots for P0 and E1 samples (d), and for E1, E2 and E3 electrodes (e). f) Normalized Fe K-edge of the N-CuHCF samples, and g,h) corresponding enlarged plot for P0 and E1 samples (g), and for E1, E2 and E3 electrodes (h).

related to the charge transfer from Fe(II) to Cu(II) through the bridging cyanide ligand. The charge transfer is not observed in E2, which contains Fe(III).

P0 and E1 in Figure 4g show similar spectral features at the Fe pre-edge region, in agreement with a Fe(II) low-spin octahedral configuration. On the other side, E2 (Figure 4h) shows evidence of Fe oxidation to its trivalent state.[53,54] Parameters retrieved from the Fe pre-edge fitting analysis are reported in Table S7, Supporting Information. Indeed, a low-intensity transition at ≈7111 eV rises at the end of the charge (see Figure S14, Supporting Information), while the transition centered ≈7114 eV shifts toward higher energies (see "Peak B′" in Figure S15, Supporting Information). In d^5 and d^6 electronic configurations in a low-spin octahedral geometry (Fe^{III} and Fe^{II}, respectively), only one transition from the core–shell to the d orbitals is allowed for Fe^{II} (transition at ≈7114 eV). In contrast, two different transitions may occur for Fe^{III}, the first one to the

partially occupied t_{2g} (transition at ≈7111 eV), the second one to an empty e_g state (at ≈7114 eV). Furthermore, due to the different effective charges of Fe^{II} and Fe^{III}, the latter transition is expected to occur at slightly higher energies for Fe^{III}. The reversible reduction of Fe^{III} to Fe^{II} takes place during the discharge, as determined by the E3 pre-edge region. In addition, the ion-insertion process is accompanied by a contraction of the lattice volume (Figure S12, Supporting Information). The Cu^I/Cu^{II} and Fe^{II}/Fe^{III} oxidation in the first charge and the Fe^{III}/Fe^{II} reduction in the discharge explain the higher specific capacity obtained in the charging process. From the XANES spectra evolution, we can also assume that only Fe is electroactive in the following cycles in the selected potential window. Ex situ XRD measurements were performed for the N-CuHCF electrodes to follow the structural evolution during the charge and discharge process. The XRD patterns of the N-CuHCF electrode were collected in the different states of charge as shown in Figure S16,
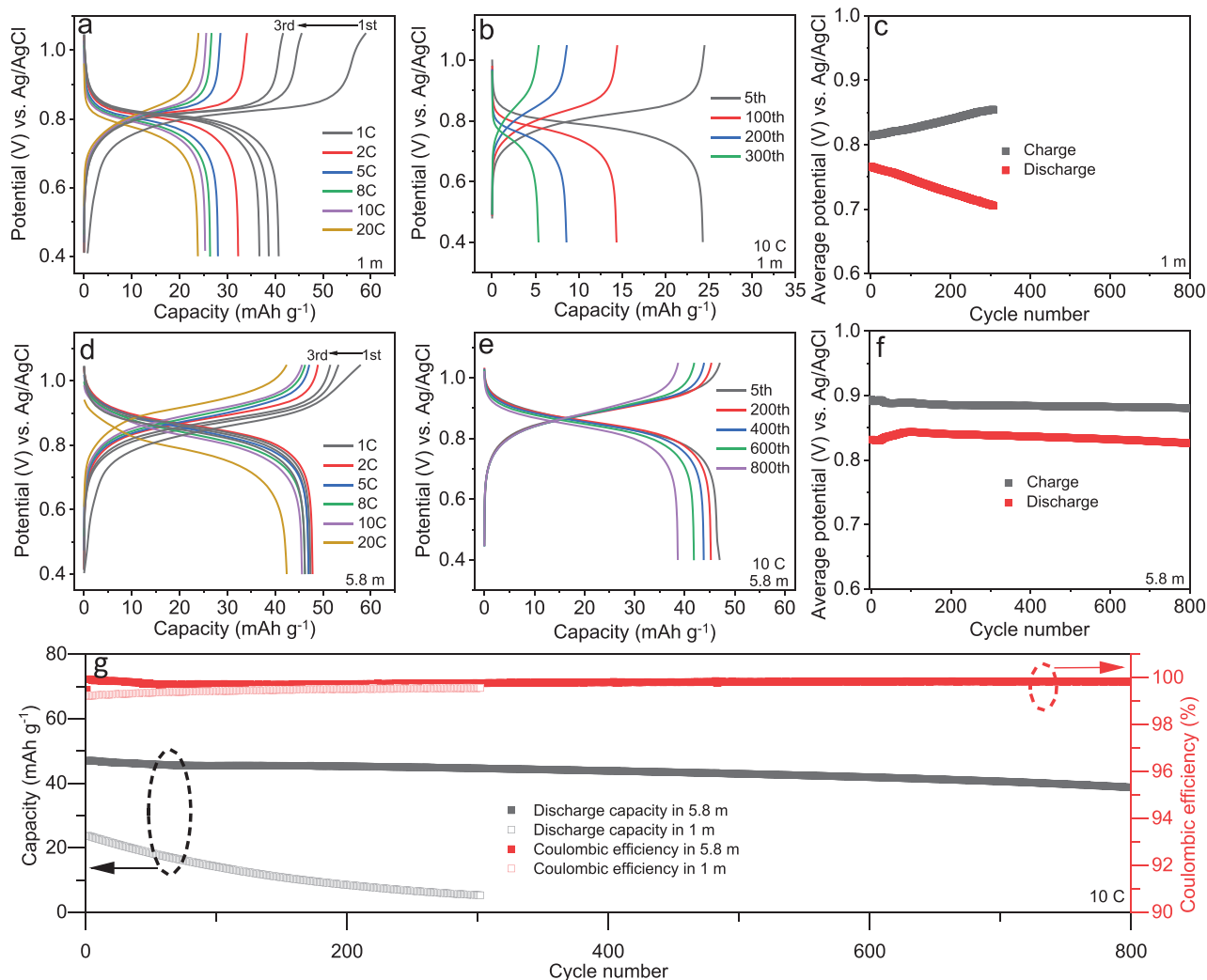
**ADVANCED
SCIENCE NEWS**

www.advancedsciencenews.com

**ADVANCED
MATERIALS**

www.advmat.de

Figure 5. a,d) Galvanostatic charge/discharge potential profiles of N-CuHCF (WE)//AC (CE) three-electrode cells (Ag/AgCl as RE) in LCE (a) and HCE (d) at 1C (60 mA g^{-1}) for the first three cycles and various rates thereafter. b,e) Selected cycles for galvanostatic charge/discharge measurement at 10C in LCE (b) and HCE (e). c,f) Evolution of average charge and discharge potential in LCE (c) and HCE (f) during long-term electrochemical cycling tests. g) Long-term cycling performance of N-CuHCF half-cells cells at 10C in LCE and HCE (see legend).

Supporting Information. The (200) peak shifted to low degrees during the de-insertion of NH$_4^+$ (charge), and then it reversibly shifted back during insertion (discharge).

Galvanostatic charge/discharge curves during the first three cycles of N-CuHCF//AC half-cells tested in LCE and HCE are shown in **Figures 5**a,d, respectively. Severe irreversible capacity and fading are seen for the cells employing the LCE electrolyte, but not for those employing HCE. The rate performance of N-CuHCF half-cells is also enhanced by this latter electrolyte, resulting in an almost doubled discharge capacity at 20 C (42.4 mA h g^{-1} versus 23.8 mA h g^{-1}). Indeed, the selected cycles of N-CuHCF half-cells employing LCE (see Figure 5b) and HCE (see Figure 5e) at 10C demonstrate that the capacity fading is more severe for those cells employing the diluted electrolyte. Moreover, the average charge/discharge potentials of N-CuHCF half-cells employing the concentrated electrolyte (see Figure 5c) appear remarkably stable and the hysteresis between the

charge/discharge is rather stable. On the contrary, N-CuHCF half-cells employing 1 M electrolyte (see Figure 5f) suffer from fast capacity fading associated with polarization. Considering that high rate cycling could mask parasitic reactions, N-CuHCF half-cells were also characterized at 0.1C (see Figure S17, Supporting Information). The cell employing LCE (Figure S17a, Supporting Information) could hardly be charged to 1.05 V (versus Ag/AgCl), while the HCE-based cell (Figure S17b, Supporting Information) could easily be charged and discharged multiple times. Despite an obvious irreversible capacity in the first cycle, the HCE-based cell could still preserve 89% of its initial discharge capacity after 20 cycles. The LCE- and HCE-cells were further characterized at 0.5C which results are shown in Figures S18a and S18c, and Figures S18b and S18d, Supporting Information, respectively. Although the LCE cell could be charged at 0.5C, it suffers from severe irreversible capacity, rapid capacity fading and low columbic efficiency (CE). On the

contrary, the HCE-based cell demonstrates limited irreversible capacity, considerable capacity retention (93%) and high CE (99.1%) after 100 cycles. The long-term cycling performance of N-CuHCF half-cells cells with HCE at 10C (see Figure 5g) demonstrates remarkable stability and a high capacity retention of 85% after 800 cycles with a high CE of 99.8%. As a comparison, the cell with 1 м electrolyte displays fast capacity fading and a poor capacity retention of 21% after 300 cycles with a maximum CE of 99.5%. After this experiment, both cells were disassembled and photographs of separators were collected, as shown in Figure S19, Supporting Information. The separator from those cells employing the 1 м electrolyte appears dark yellow because of the dissolution of N-CuHCF, while the separator from cells using the HCE remains white, indicating that N-CuHCF is rather stable in the concentrated electrolyte.

To assess the influence of mass loading and electrode thickness on the cell performance, N-CuHCF electrodes with increasing thickness were prepared and characterized (see Figure S20a, Supporting Information). The active material mass loading and thickness of electrodes denoted as H30, H60, H90 and H120 were ≈0.9, ≈1.2, ≈1.5 and ≈1.7 mg cm^{-2} and 15, 21, 26 and 30 µm, respectively. Scanning electron microscopy (SEM) images for H30 (Figure S20b, Supporting Information), H60 (Figure S20c, Supporting Information), H90 (Figure S20d, Supporting Information), and H120 (Figure S20e, Supporting Information) were also collected. Among these four electrodes, H60 displays the most homogenous surface, while large cracks can be observed on H120. Therefore, this thicker sample was excluded from further characterization. The three electrodes H30, H60 and H90 were first activated at 1C for four cycles and subsequently cycled at 2C in HCE (see Figure S21, Supporting Information). As a result, the H60 displays the most stable cycling performance and highest coulombic efficiency. After such measurements, the cells were disassembled, and photographs of the separators were taken (see Figure S22, Supporting Information). The separator extracted from the cell with H60 displays the lightest color compared with the other two, indicating reduced active material dissolution. In addition, a calendar life test was carried out in HCE (see Figure S23, Supporting Information). The cell was cycled for 100 cycles first and, afterward, stored for 3 weeks at discharged state before resuming the cycling test. Notably, the cell could still provide consistent electrochemical performance with only very limited capacity fading.

Among multiple guest ions, PBAs have the capability to host protons too.[55] To investigate the effect of proton insertion on PBAs, a H_2SO_4 solution having the same pH value (5.3) and a concentration of ≈2.5 × 10^{-6} mol L^{-1} was prepared and used as control electrolyte. As shown in Figure S24a, Supporting Information, the cells with H_2SO_4 electrolyte could be regularly cycled. The host material could well accommodate both ammonium ions and protons, but the insertion of NH_4^+ occurs at more positive potentials compared to protons (from 0.90 to 0.75 V instead of 0.75–0.6 V for proton insertion). This means that, despite the competition between the two processes, ammonium ions will first occupy the insertion sites during discharge and proton insertion will become negligible. Meanwhile, the galvanostatic charge/discharge measurement of N-CuHCF half-cells with H_2SO_4 solution at 10 C shows severe

capacity fading (see Figure S24b, Supporting Information). The corresponding long-term cycling performance (see Figure S24c, Supporting Information) is also poor and capacity retention of 66% with a CE of 97% can be obtained after ≈70 cycles. Therefore, although proton and ammonium insertion processes can be in competition, the outstanding performance of N-CuHCF half cells with HCE is certainly associated with the concentrated NH_4^+ electrolyte. To further investigate the effect of pH values of HCE on the cell performance, HCE with different pH values are prepared by addition of H_2SO_4 in different amounts to tune the pH values at 1.15, 2.15, 3.03 and 4.01, which are denoted as HCE-1, HCE-2, HCE-3 and HCE-4, respectively (see Table S8, Supporting Information). The long-term cycling tests (see Figure S25, Supporting Information) show that both HCE-3 and HCE-4 could enable stable cell cycling and high CE. When the pH of the electrolyte is decreased (see HCE-2 and HCE-1), both coulombic efficiency and capacity retention gradually worsen.

F 1s, O 1s, N 1s, and S 2p XP spectra of N-CuHCF electrodes cycled in LCE (see **Figure 6**a) and HCE (see Figure 6c) were collected to investigate the chemical composition of the electrode surface after cycling. First, the surface layer thickness is linked with the electrolyte concentration. In fact, the electrode's surface appears covered by a thinner layer when using the LCE, as indicated by the presence of feature related to the electrode components such as, $-CF_2-$ from PVDF (at 687.8 eV in F 1s), and $-Cu-N-C-$ from the active material (at ≈398 eV in N 1s),[56] which are not seen on the electrode cycled in the HCE. The surface layer grown in the 1 м electrolyte is composed mainly of $(NH_4)_2SO_4$ salt as indicated by the peaks in the N 1s spectrum at 402 eV, which corresponds to the NH_4^+ cation, and the S 2p, corresponding to $-SO-$ from SO_4^{2-} anion. In addition, carbonates ($-C=O$) and hydroxides (NH_4OH, but might be also $Cu(OH)_2$ or $Fe(OH)_2$ due to the solubility of the N-CuHCF in the electrolyte) are observed, resulting from the O_2 and CO_2 dissolved in the electrolyte, as well as from the interaction of the electrode materials with air and moisture.[49,57,58]

The similar shape of the XPS spectra after 5 and 10 min of sputtering, and the only minor differences in at% concentration of the detected elements (see Figure 5a,b) indicate that the composition of the electrode surface is quite homogenous. Most interestingly, the Fe 2p and Cu 2p XPS spectra (see Figure S26, Supporting Information) of the electrode cycled in 1 м electrolyte indicate that the amount of Fe increases at higher depths. Specifically, the XPS peak at ≈935 and ≈944 eV for Cu 2p as detected on the electrode surface (see Figure S26, Supporting Information) could be attributed to copper sulfate,[59] indicating the occurrence of a severe reaction between the active material (N-CuHCF) and 1 м $(NH_4)_2SO_4$.

SEM/FIB was performed to better understand the morphological and chemical composition of electrodes cycled in LCE and HCE. The SEM image of the pristine N-CuHCF electrode (**Figure 7**a-I) shows a porous, but uniform surface. However, the surface of the N-CuHCF electrode cycled in LCE (Figure 7b-I) appears slightly rougher and with some additional deposits. Interestingly, the surface of the N-CuHCF electrode cycled in HCE (Figure 7c-I) appears to be covered by an in situ formed layer. To further investigate the electrode surface and bulk, cross-sectional SEM images of the pristine and
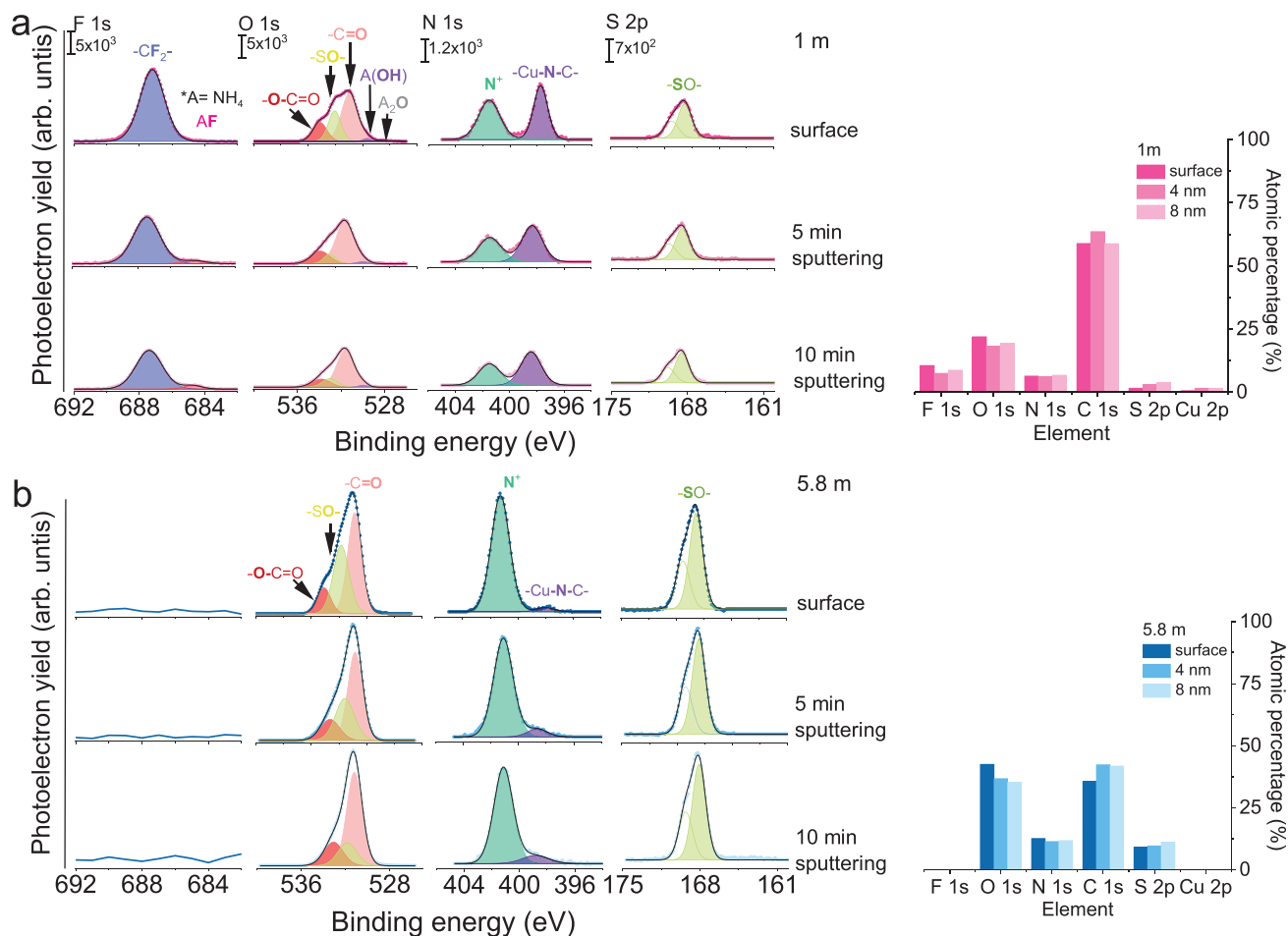
**ADVANCED
SCIENCE NEWS**

www.advancedsciencenews.com

**ADVANCED
MATERIALS**

www.advmat.de

Figure 6. a,c) F 1s, O 1s, N 1s, and S 2p XP spectra of N-CuHCF electrodes cycled in LCE (a) and HCE (c). b,d) Corresponding elemental distribution (at%) on the surface of N-CuHCF electrodes cycled in LCE (b) and HCE (d).

cycled electrodes were collected after cutting the samples by FIB. The cross-sectional SEM image of the pristine electrode (Figure 7a-II) reveals a very porous structure. For the electrode cycled in LCE, the electrode porosity appears filled by a dense substance, which becomes more abundant closer to the current collector (Figure 7b-II). Interestingly, the porosity of the electrode cycled in HCE is almost totally filled (Figure 7c-II). Afterward, EDX was performed to gain elemental information about all three electrodes. The EDX mapping images of pristine electrode showed some C-rich island (Figure 7a-IV) most likely attributable to the conductive additive (Super C65) and PVDF binder. The Cu (Figure 7a-V) and Fe (Figure 7a-VI) maps demonstrate the homogeneous distribution of the active material. In comparison, EDX mapping images of the electrode cycled in LCE show that C (Figure 7b-IV), Cu (Figure S27a-I, Supporting Information), and Fe (Figure S27a-II, Supporting Information) are uniformly distributed throughout the whole electrode depth. Most interestingly though, S- (Figure 7b-V) and O-rich (Figure 7b-VI) regions are found at the bottom of the electrode. The limited anodic stability of LCE (see Figure 2a) would lead to the water decomposition when the cells are charged to 1.05 V (versus Ag/AgCl), causing precipitation of the salt in the close

proximity of the current collector. EDX maps of the electrode cycled in HCE demonstrate rather different features. Namely, the content of C (Figure 7c-IV), Cu (Figure S27b-I, Supporting Information) and Fe (Figure S27b-II, Supporting Information) appear weaker compared with that for electrode cycled in LCE, which may be hidden by the newly formed surface layer. Moreover, S (Figure 7c-V) and O (Figure 7c-VI) are uniformly distributed on the whole electrode depth. Additionally, a very dense S- and O- containing layer (with ≈3 µm thickness) could be detected on the electrode surface. These results suggest that, despite the enhanced anodic stability of HCE, the salt can also precipitate in this nearly-saturated electrolyte after hundreds of cycles, as a result of water decomposition under the catalytic effect. Such a salt precipitate would, however, gather preferentially on the electrode surface (i.e., the interface with the electrolyte) rather than at the current collector interface. According to the electrochemical results previously described, this phenomenon does not appear to be detrimental. Instead, such surface layer may help to exclude water from the electrode, granting its long-term stable performance. In order to prove this, electrochemical impedance spectroscopy (EIS) tests were performed upon cycling. The cells employing HCE (see
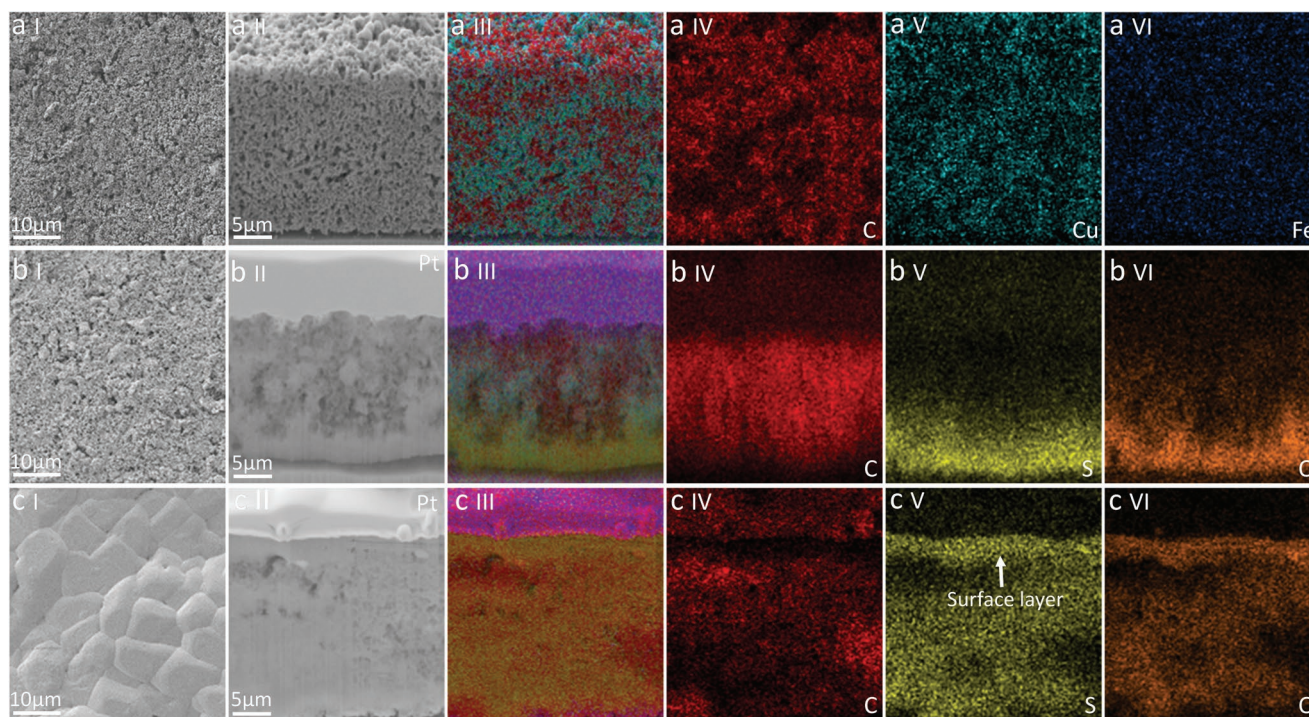
Figure 7. a–c) SEM (top view) of N-CuHCF electrodes as made (a-I) and after cycling in LCE (b-I) and HCE (c-I). Cross-sectional SEM images of a pristine N-CuHCF electrode (a-II) after FIB milling and the corresponding EDX mapping images (a-III–VI). Cross-sectional SEM images of the electrodes cycled in LCE (b-II) and HCE (c-II) after FIB milling, and the corresponding EDX mapping images of the electrode cycled in LCE (b-III–VI) and HCE (c-III–VI).

Figure S29, Supporting Information) evidence a very stable response compared to those employing LCE (see Figure S28, Supporting Information). This demonstrates that, even in case of partial precipitation of the salt, the properties of the electrode/electrolyte interface are not detrimentally affected.

Galvanostatic charge/discharge curves of PTCDI half-cells with LCE and HCE at 1C for the first three cycles are shown in **Figures 8**a,d, respectively. The PTCDI half-cells employing LCE suffer a large irreversible capacity, probably due to H_2 evolution at the low cut-off voltage (−1 V versus Ag/AgCl) during the discharge process. The occurrence of H_2 evolution is, in fact, consistent with the result from the cathodic scan of LSV measurement (see Figure 2a). As expected, the irreversible capacity and H_2 evolution are suppressed in HCE. Indeed, although the reversibility improves at high currents, the PTCDI half-cells cycled in LCE still show substantial irreversible capacity (see Figure 8a). In contrast, as demonstrated by the data shown in Figure 8d, high reversibility is maintained when HCE is employed, even at low current density. The mechanism of NH_4^+ insertion into PTCDI in aqueous electrolyte was already proposed by Ji's group. Specifically, the two reversible charge/discharge plateaus can be attributed to the reversible evolution of the carbonyl groups in PTCDI.[60] Long-term cycling measurements were also performed for PTCDI half-cells with LCE and HCE at 5C. PTCDI half-cells with LCE showed a noticeable capacity fading and low CE as seen from the selected voltage profiles (Figure 8b) and the long-term cycling (Figure 8c). Promisingly, PTCDI half-cells cycled in HCE exhibit considerably enhanced cycling stability without

obvious potential or capacity decay (see Figure 8e). As shown in Figure 8f, PTCDI half-cells with HCE display a capacity of ca. 100 mAh g⁻¹ after 5000 cycles, which corresponds to ≈98% retention, with a CE of 99.9%. Additionally, the long-term cycling performance at 10C was also investigated (Figure 8g) for PTCDI half-cells cells in the HCE. Impressively, the cells delivered 79 mAh g⁻¹ at 10 C with a capacity retention of 89% and a CE of 99.9% after 45 000 cycles. After the long-term cycling experiments, the cells cycled in both electrolytes were disassembled and pictures of the separators were collected (see Figure S30, Supporting Information). While the separator from the cell using 1 M electrolyte shows a dark purple coloration because of the dissolution of PTCDI, the one from the cell using the HCE is just slightly colored, suggesting suppressed dissolution. Considering that the high rate could mask parasitic reactions, PTCDI half-cells were tested at 0.1C in LCE (see Figure S31a, Supporting Information) and HCE (see Figure S31b, Supporting Information). The cell with LCE could not be discharged to −1.0 V (versus Ag/AgCl) as a possible result of hydrogen evolution while the cell with HCE could be regularly operated. Despite the reduced CE (91.7%), the HCE-based cell delivered a relatively stable capacity for 50 cycles. To investigate the effect of proton insertion on PTCDI electrode, a H_2SO_4 solution with the pH value of 5.3, (as previously done with the PBAs electrode) was used as ammonium-free electrolyte. However, massive electrolyte decomposition hinders the discharge to −1.0 V (versus Ag/AgCl) (see Figure S32, Supporting Information), suggesting that such acidic electrolyte is incompatible with PTCDI.
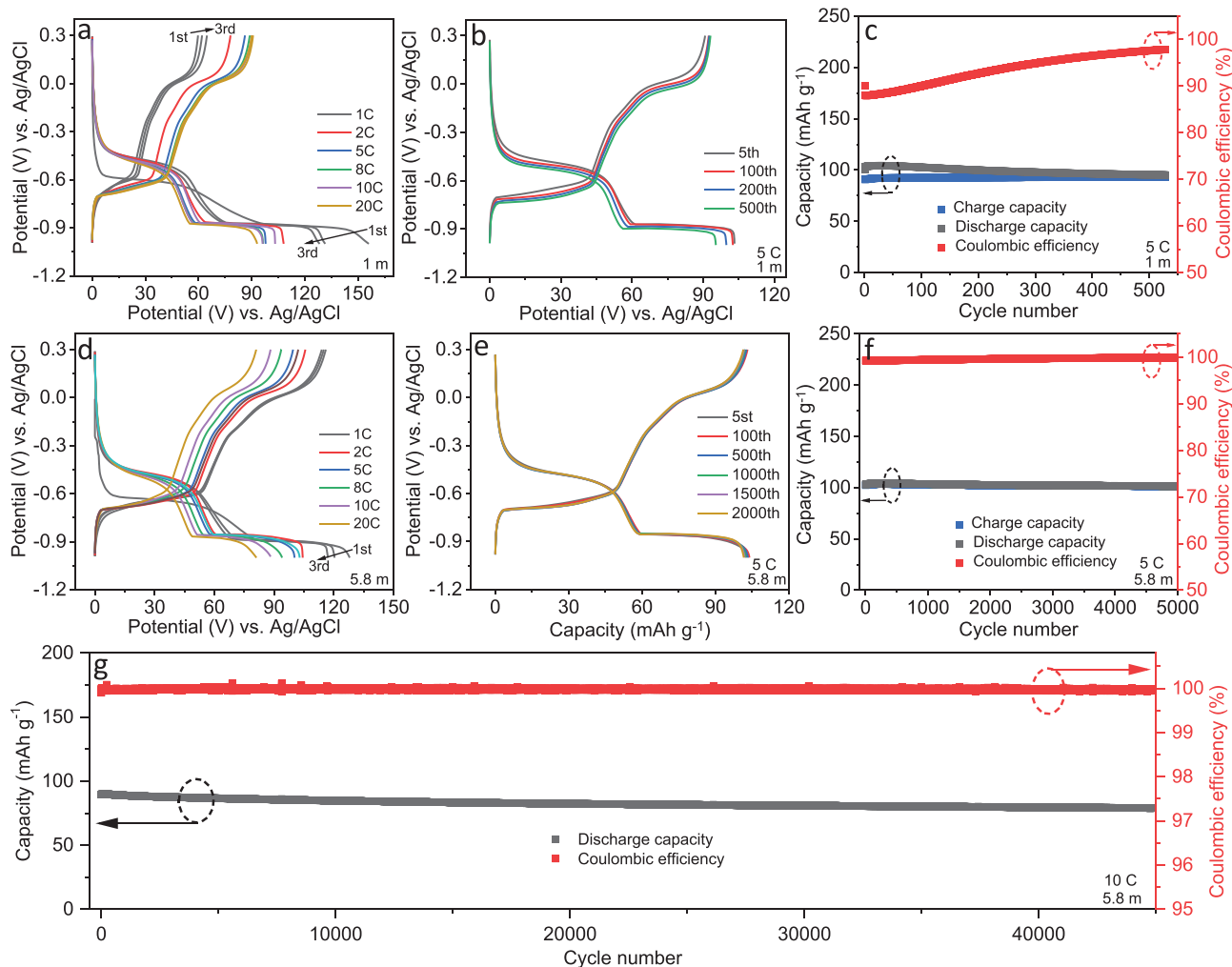
Figure 8. a,d) Galvanostatic charge/discharge curves in LCE (a) and HCE (d) at 1C (120 mA g⁻¹) for the first three cycles and the corresponding rate capability in three-electrode Swagelok T-cells employing PTCDI as working electrode, an Ag/AgCl as reference electrode and self-standing AC as counter electrode. b,e) The selected cycles for galvanostatic charge/discharge measurement at 5C in LCE (b) and HCE (e). c,f) Long-term cycling performance of PTCDI half-cells with LCE (c) and HCE (f) at 5C. g) Long-term cycling performance of PTCDI half-cells with HCE at 10C.

PTCDI//N-CuHCF full cells with HCE electrolyte were assembled, following the promising electrochemical performance of the N-CuHCF cathode and the PTCDI anode in half-cells. As shown in **Figure 9**a, the cathode and anode can be well integrated together to support a full aqueous cell with a high operative voltage range (0.4–2.0 V). PTCDI//N-CuHCF full-cells with HCE at 5C delivered a discharge capacity of 48.2 mAh g⁻¹ calculated based on the N-CuHCF cathode mass (see Figure 9b). After the second cycle, the discharge capacity remains stable. The full-cells show a remarkable rate performance and a discharge capacity of 39.3 mAh g⁻¹ could be achieved at 20C (see Figure 9c), which could be attributed to the fast mobility of NH_4^+ ions. Finally, the long-term cycling performance of the full-cells was evaluated at 10C (see Figure 9d) and capacity retention of ≈72% could be obtained over 1000 cycles with a CE of 99.2% and an average discharge voltage of ≈1 V. To compare the electrochemical performance of the full rocking-chair AAIBs presented in this work with similar systems reported in the previous literature, some of the most relevant performance metrics

are summarized in Table S9, Supporting Information. The full AAIB proposed here features among the highest average output voltage (≈1 V) and high CE (99.2%) at the same time, although the capacity retention could be further improved. The specific energy and power of such a system with inactive components are estimated to be ≈31 Wh kg⁻¹ and ≈443 W kg⁻¹, respectively. Moreover, the electrode materials used in this work just include low-cost and eco-friendly elements.

3. Conclusion

The highly concentrated (5.8 M) solution of $(NH_4)_2SO_4$ in water (HCE) has been characterized and employed as electrolyte for AAIBs. Classical MD simulations and SWAXS were performed to fully understand the solvation structure of such a concentrated electrolyte, including the comparison with the diluted LCE. HCE provides a larger ESW enabling the highly reversible insertion/de-insertion of NH_4^+ into the N-CuHCF cathode

**ADVANCED
SCIENCE NEWS**

www.advancedsciencenews.com
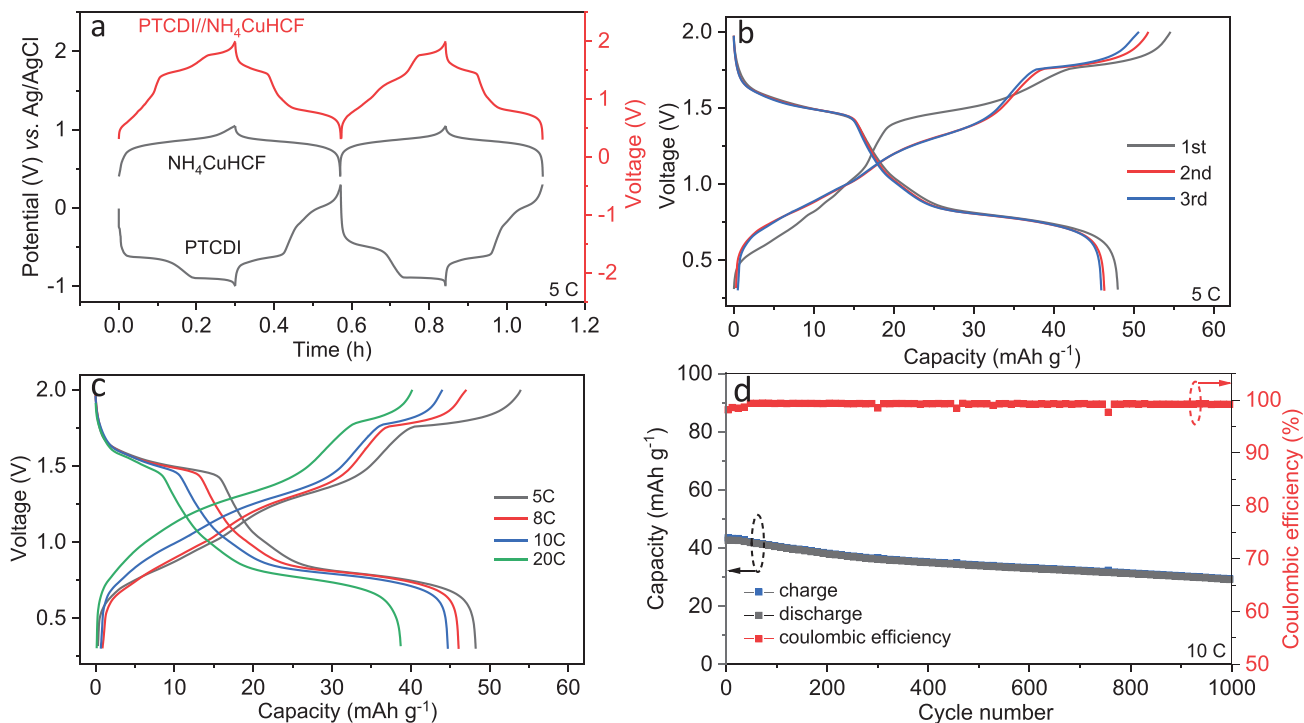
**ADVANCED
MATERIALS**

www.advmat.de

Figure 9. a) Galvanostatic charge/discharge curves during the initial two cycles of N-CuHCF half-cell, PTCDI half-cell, and PTCDI//N-CuHCF full cell with HCE at 300 mA g^{-1}. Galvanostatic charge/discharge curves of PTCDI//N-CuHCF full cells with HCE. b) Initial three cycles at 5C and c) during the following rate performance tests. d) Long-term cycling performance of the same full cell at 10C.

and PTCDI anode. XANES results demonstrated the reversible redox reaction of Fe^{2+}-CN-/Fe^{3+}-CN- during NH$_4^+$ uptake/release. The concentrated electrolyte enabled N-CuHCF cathode and PTCDI anode stable long-term cycling, which is attributed to less dissolution of active materials. Finally, PTCDI//N-CuHCF full-cells were assembled and tested, demonstrating high capacity retention (72% over 1000 cycles) with a considerable CE (99.2%) and a high average output voltage (≈1 V).

4. Experimental Section

Materials Preparation: The N-CuHCF cathode material was prepared as previously reported in the literature.[24] First, copper hexacyanoferrate (CuHCF) was synthesized by a co-precipitation method. Concretely, 40 mL of 40 × 10^{-3} M Cu(NO$_3$)$_2$ (Alfa Aesar) and 40 mL of 20 × 10^{-3} M K$_3$Fe(CN)$_6$ (Sigma Aldrich) were reacted by simultaneous, dropwise addition into water (100 mL) under vigorous stirring. Five minutes after the combination of the CuHCF precursors, 0.1 M Na$_2$S$_2$O$_3$ was added until the color of CuHCF changed from dingy yellow to deep red. The CuHCF containing sodium and potassium cations was filtered and washed with deionized (DI) water, and further dried in a vacuum at room temperature. Afterward, N-CuHCF was prepared by an ion-exchange method, in which the sodium and potassium were replaced by NH$_4^+$. Briefly, 1 g CuHCF was dispersed by stirring for 6 h in 40 mL of 1 M (NH$_4$)$_2$SO$_4$ solution. After that, the as-obtained precipitates were washed with DI water 3 times and dried in an oven at 60 °C. The 4,9,10-perylenetetracarboxylic diimide (PTCDI) was purchased from Sigma Aldrich and used without any purification. In fact, PTCDI is proved to be a viable host material for reversible storage of NH$_4^+$ by ex situ XRD in the previous literature.[24] The LCE and HCE electrolytes were prepared by dissolving 1 mol and 5.8 mol of (NH$_4$)$_2$SO$_4$ in 1 kg of DI water, respectively.

Computational Details: Molecular dynamics simulations were carried out using Amber 18 software[61] exploiting the GAFF force field.[62] The atomic partial charges were obtained with the RESP algorithm from DFT calculations run with Gaussian09e[63] at the B3LYP/6-311++G** level of theory. The starting random molecular arrangements were obtained by Packmol[64] in boxes with sides of ≈60 Å. The simulation went through different steps starting from a geometrical relaxation, followed by a gradual heating of the system from 0 to 50 K in several NVT sessions. The systems where then equilibrated at 300K for 20 ns in NPT ensemble, and for a further 20 ns in NVT. A final productive NVT phase of 10 ns was then used for the analysis. For the productive phase, the timestep used was 2 fs, and the simulation was dumped every 1000 steps, obtaining a final trajectory of 5000 frames spaced by 2 ps each. The trajectories were analyzed with Travis.[65,66]

Characterization: The SWAXS patterns were collected using a Xeuss 3.0c (Xenocs, Grenoble, France) equipped with an Eiger2 1M detector. The Sample-to-Detector distance was set to 100 mm. A Cu K$_\alpha$ source was exploited with a beam size of 0.7 × 0.7 mm^2, obtaining a flux of ≈10^8 photons/s. The samples were injected in 1.5 mm (outer diameter) borosilicate capillaries and sealed with solventless hot glue. The sample chamber of the instrument was kept under vacuum (P = 50 µbar) during the experiment. Each sample was exposed for 10 min to X-rays to ensure a good signal-to-noise ratio. The empty capillary background was also collected and subtracted from the total scattering curve. Data treatment was performed with the Xsact software from Xenocs, PDFgetX3, and some in-house MATLAB code. Thermal analysis was performed employing a differential scanning calorimetry (DSC) (Discovery TA) calorimeter. Samples (≈8 mg) were loaded into gold pans, which were hermetically sealed. The samples were first cooled down from 20 to −80 °C, and then heated up to 60 °C at a rate of 10 °C min^{-1}. Finally, the samples were cooled down from 60 to 20 °C at the same rate.

X-ray diffraction (XRD) patterns were recorded using a Bruker D8 diffractometer equipped with a Cu K$_\alpha$ source (λ = 0.15406 nm) in the 5° < 2θ < 140° range with step size of 0.01° and 5 s per point

acquisition time. Rietveld refinement of the powder was conducted using GSAS-II software.[67] The structural model reported by Ojwang et al.[68] was modified according to the stoichiometry obtained of the hexacyanoferrate materials by ICP-OES. Furthermore, the structural reference model, obtained using synchrotron radiation, was simplified to consider a laboratory diffractometer's lower degree of accuracy. For this reason, the interstitial ions were considered to occupy the *8c* Wyckoff positions on average. The background was fitted with a Chebyshev polynomial function with six coefficients. The instrumental parameters were obtained from the LaB_6 standard. Accordingly, the instrumental broadening parameters, that is, U, V, W, X and Y, were kept fixed to 4.397×10^{-4} deg^2, -5.720×10^{-4} deg^2, 2.577×10^{-4} deg^2, 1.855×10^{-2} deg and 2×10^{-5} deg, respectively. The peak shape was refined with an isotropic particle size broadening model and by optimizing the respective parameter. The scale, background, sample displacement, unit cell parameters, peak shape and atomic parameters were refined in this order. Sequential Rietveld refinement of the in situ datasets was performed in the $22.5° < 2\theta < 80°$ range by considering as the structural model the one obtained for the N-CuHCF powder and by fixing the atomic parameters. The instrumental parameters were kept fixed to the respective powder's values, while the peak shape was refined by optimizing the isotropic particle size parameter. The scale, background, unit cell parameters, and peak shape were refined in this order.

XANES experiments were carried out at the B18 beamline[69,70] of Diamond Light Source (UK) under the Block Allocation Group (BAG). Data treatment was carried out with the Athena software within the Demeter package.[71] The pristine N-CuHCF powder (P0) was well mixed with cellulose as a filler and pressed into a pellet. For the electrode samples (E1, E2 and E3), N-CuHCF powder, carbon black (Super C65, IMERYS), and PTFE as a binder were well mixed in the 7:2:1 weight ratio and processed into a self-standing film. DI water was used as a solvent for this process. Then, the self-standing film was coated on a Ti mesh (nominal aperture 0.19 mm, thickness 0.46 mm, purity 99.6%, Goodfellow, USA) and cut into a round disk with a diameter of 12 mm after pressing it at 2 ton m^{-2}. After that, the electrodes were further dried at 120 °C under a high vacuum (10^{-4} mbar). The active material loading was ≈5 mg cm^{-2} to obtain an optimal absorption signal. The electrodes were used as the working electrode in three-electrode Swagelok cells comprising self-standing activated carbon (AC) as the counter electrode, a leakless Ag/AgCl reference electrode, and HCE as the electrolyte. Galvanostatic charge/discharge tests were carried out and stopped at the selected state of charge. Finally, the cells were disassembled and the electrodes were collected and dried at 120 °C in a vacuum oven. Finally, all samples were sealed in polyethylene (PE) bags to avoid exposure to air.

The morphology and composition of samples was investigated by SEM using the ZEISS Crossbeam XB340. The XPS measurements were performed for the Ti current collectors at OCV, 0.9 and 1.2 V during the LSV measurement in LCE and HCE. The cycled N-CuHCF electrodes employing both electrolytes (1 and 5.8 M) are also investigated by XPS. It should be noted that the samples for SEM and XPS measurements were not washed because the formed substances on the surface can be easily removed. However, by prolonged Ar$^+$ sputtering it was possible to access and probe the inner part of the samples. A monochromatic Al-K$_\alpha$ ($h\nu$ = 1486.6 eV) X-ray source and a Phoibos 150 XPS spectrometer, in fixed transmission mode, were used. High-resolution scans were acquired at 200 W, 30 eV pass energy, and 0.1 eV energy step. Additionally, the depth profiling was carried out by a focused ion gun with 5 kV Ar$^+$ with an ion filter at two different sputtering times (5 and 10 min). The calibration of the photoelectron spectra was carried out using the graphitic-like carbon peak at 284.4 eV as a reference. The fits were performed with the CasaXPS software, using a nonlinear Shirley-type background and a 70% Gaussian and 30% Lorentzian profile function. Thermogravimetric analysis (TGA) was carried out with TA Instruments (Model Q5000) under a nitrogen flow using a temperature ramp of 5 °C min^{-1} from 30 to 800 °C. IR spectra were acquired from powders and electrodes with a MAGNA FTIR-750-Nicolet spectrometer.

Electrochemical Measurements: LSV measurements on bare Ti foil (thickness 0.025 mm, purity 99.9%, Goodfellow, USA) of $(NH_4)_2SO_4$ aqueous solutions at different concentration were carried out in three-electrode glass cells, which comprised Ti foil as the working electrode, a Pt-coated Ti (Pt/Ti) rod as the counter electrode, and a leakless Ag/AgCl as the reference electrode (sat. KCl, 0.197 V versus SHE). Both N-CuHCF and PTCDI electrodes were prepared by casting slurries constituted by 80 wt% N-CuHCF or PTCDI, 15 wt% carbon black (Super C65, IMERYS Graphite & Carbon), and 5 wt% polyvinylidene fluoride (PVDF) (Solef 6020, Arkema Group) on Ti foil current collectors. *N*-Methyl-2-pyrrolidone (anhydrous, Sigma-Aldrich) was used to prepare all slurries. After drying at room temperature, electrodes with a diameter of 12 mm for N-CuHCF and PTCDI were punched and further dried at 120 °C under high vacuum overnight. The average active material mass loading was ≈1.2 mg cm^{-2} for N-CuHCF electrodes and 1.0 mg cm^{-2} for PTCDI electrodes, which were used for half-cell measurements. For assembling full-cells, the PTCDI negative electrodes had a mass loading of 0.6 mg cm^{-2} to match the N-CuHCF positive electrodes, meaning that the p/n capacity ratio was ≈1.06. The counter electrode used in the three-electrode cells were self-standing films of activated carbon, composed of 70 wt% activated carbon (AC, YP50 from Kuraray), 20 wt% Super C65 and 10 wt% PTFE as binder. Cyclic voltammetry (CV), galvanostatic charge–discharge, and long-term cycling measurements in half-cell configuration were performed in three-electrode Swagelok-like cells consisting of N-CuHCF or PTCDI as the working electrode, a self-standing activated carbon (AC) as counter electrode, and leakless Ag/AgCl as the reference electrode. The long-term, galvanostatic cycling measurements of N-CuHCF//PTCDI cells were carried out in two-electrode Swagelok-like cells. The working and counter electrodes in all Swagelok-like cells were separated by glass microfiber separator discs (Whatman Grade GF/A; diameter of 13 mm), while a glass microfiber separator disc (Whatman Grade GF/D; diameter of 10 mm) was utilized to separate the reference electrode when present. The activated carbon counter electrodes were largely oversized. LSV and CV tests were conducted with a multi-channel potentiostat/galvanostat (VMP3, Biologic Science Instruments, France). A Maccor 4000 Battery system (Maccor, USA) was used for the galvanostatic charge/discharge test at various C-rates at 20 °C.

Supporting Information

Supporting Information is available from the Wiley Online Library or from the author.

Acknowledgements

Conflict of Interest

The authors declare no conflict of interest.

[1] Z. Yang, J. Zhang, M. C. Kintner-Meyer, X. Lu, D. Choi, J. P. Lemmon, J. Liu, *Chem. Rev.* **2011**, *111*, 3577.

[2] D. Larcher, J.-M. Tarascon, *Nat. Chem.* **2015**, *7*, 19.

[3] G. Crabtree, *Nature* **2015**, *526*, S92.

[4] X. Zeng, J. Hao, Z. Wang, J. Mao, Z. Guo, *Energy Storage Mater.* **2019**, *20*, 410.

[5] B. Dunn, H. Kamath, J.-M. Tarascon, *Science* **2011**, *334*, 928.

[6] K. Liu, Y. Liu, D. Lin, A. Pei, Y. Cui, *Sci. Adv.* **2018**, *4*, eaas9820.

[7] O. Schmidt, A. Hawkes, A. Gambhir, I. Staffell, *Nat. Energy* **2017**, *2*, 17110.

[8] D. Chao, W. Zhou, F. Xie, C. Ye, H. Li, M. Jaroniec, S.-Z. Qiao, *Sci. Adv.* **2020**, *6*, eaba4098.

[9] Y. Wang, J. Yi, Y. Xia, *Adv. Energy Mater.* **2012**, *2*, 830.

[10] W. Li, J. R. Dahn, D. S. Wainwright, *Science* **1994**, *264*, 1115.

[11] L. Suo, O. Borodin, T. Gao, M. Olguin, J. Ho, X. Fan, C. Luo, C. Wang, K. Xu, *Science* **2015**, *350*, 938.

[12] C. D. Wessells, S. V. Peddada, R. A. Huggins, Y. Cui, *Nano Lett.* **2011**, *11*, 5421.

[13] Y. Wang, L. Mu, J. Liu, Z. Yang, X. Yu, L. Gu, Y. S. Hu, H. Li, X. Q. Yang, L. Chen, *Adv. Energy Mater.* **2015**, *5*, 1501005.

[14] Z. Li, D. Young, K. Xiang, W. C. Carter, Y.-M. Chiang, *Adv. Energy Mater.* **2013**, *3*, 290.

[15] J. Han, A. Mariani, H. Zhang, M. Zarrabeitia, X. Gao, D. V. Carvalho, A. Varzi, S. Passerini, *Energy Storage Mater.* **2020**, *30*, 196.

[16] D. Su, A. McDonagh, S. Z. Qiao, G. Wang, *Adv. Mater.* **2017**, *29*, 1604007.

[17] N. Zhang, F. Cheng, J. Liu, L. Wang, X. Long, X. Liu, F. Li, J. Chen, *Nat. Commun.* **2017**, *8*, 405.

[18] H. Pan, Y. Shao, P. Yan, Y. Cheng, K. S. Han, Z. Nie, C. Wang, J. Yang, X. Li, P. Bhattacharya, K. T. Mueller, J. Liu, *Nat. Energy* **2016**, *1*, 16039.

[19] B. Tang, L. Shan, S. Liang, J. Zhou, *Energy Environ. Sci.* **2019**, *12*, 3288.

[20] X. Sun, V. Duffort, B. L. Mehdi, N. D. Browning, L. F. Nazar, *Chem. Mater.* **2016**, *28*, 534.

[21] F. Wang, X. Fan, T. Gao, W. Sun, Z. Ma, C. Yang, F. Han, K. Xu, C. Wang, *ACS Cent. Sci.* **2017**, *3*, 1121.

[22] R. Y. Wang, C. D. Wessells, R. A. Huggins, Y. Cui, *Nano Lett.* **2013**, *13*, 5748.

[23] C. Wu, S. Gu, Q. Zhang, Y. Bai, M. Li, Y. Yuan, H. Wang, X. Liu, Y. Yuan, N. Zhu, *Nat. Commun.* **2019**, *10*, 73.

[24] X. Wu, Y. Qi, J. J. Hong, Z. Li, A. S. Hernandez, X. Ji, *Angew. Chem., Int. Ed.* **2017**, *56*, 13026.

[25] J. Han, A. Varzi, S. Passerini, *Angew. Chem., Int. Ed.* **2022**, 61, e202115046.

[26] C. D. Wessells, S. V. Peddada, M. T. McDowell, R. A. Huggins, Y. Cui, *J. Electrochem. Soc.* **2012**, *159*, A98.

[27] M. R. Lukatskaya, O. Mashtalir, C. E. Ren, Y. Dall'Agnese, P. Rozier, P. L. Taberna, M. Naguib, P. Simon, M. W. Barsoum, Y. Gogotsi, *Science* **2013**, *341*, 1502.

[28] X. Zhang, M. Xia, H. Yu, J. Zhang, Z. Yang, L. Zhang, J. Shu, *Nano-Micro Lett.* **2021**, *13*, 139.

[29] X. Zhang, M. Xia, T. Liu, N. Peng, H. Yu, R. Zheng, L. Zhang, M. Shui, J. Shu, *Chem. Eng. J.* **2021**, *421*, 127767.

[30] M. Xia, X. Zhang, H. Yu, Z. Yang, S. Chen, L. Zhang, M. Shui, Y. Xie, J. Shu, *Chem. Eng. J.* **2021**, *421*, 127759.

[31] S. Dong, W. Shin, H. Jiang, X. Wu, Z. Li, J. Holoubek, W. F. Stickle, B. Key, C. Liu, J. Lu, P. A. Greaney, X. Zhang, X. Ji, *Chem* **2019**, *5*, 1537.

[32] J. J. Holoubek, H. Jiang, D. Leonard, Y. Qi, G. C. Bustamante, X. Ji, *Chem. Commun.* **2018**, *54*, 9805.

[33] W. Xu, L. Zhang, K. Zhao, X. Sun, Q. Wu, *Electrochim. Acta* **2020**, *360*, 137008.

[34] G. Liang, Y. Wang, Z. Huang, F. Mo, X. Li, Q. Yang, D. Wang, H. Li, S. Chen, C. Zhi, *Adv. Mater.* **2020**, *32*, 1907802.

[35] D. Yu, Z. Wei, X. Zhang, Y. Zeng, C. Wang, G. Chen, Z. X. Shen, F. Du, *Adv. Funct. Mater.* **2021**, *31*, 2008743.

[36] H. Li, J. Yang, J. Cheng, T. He, B. Wang, *Nano Energy* **2020**, *68*, 104369.

[37] Q. Chen, J. Jin, M. Song, X. Zhang, H. Li, J. Zhang, G. Hou, Y. Tang, L. Mai, L. Zhou, *Adv. Mater.* **2022**, *34*, 2107992.

[38] Y. Song, Q. Pan, H. Lv, D. Yang, Z. Qin, M. Y. Zhang, X. Sun, X. X. Liu, *Angew. Chem.* **2021**, *133*, 5782.

[39] S. Qiu, Y. Xu, X. Li, S. K. Sandstrom, X. Wu, X. Ji, *Electrochem. Commun.* **2021**, *122*, 106880.

[40] S. F. Kuchena, Y. Wang, *ACS Appl. Energy Mater.* **2020**, *3*, 11690.

[41] Z. Tian, V. S. Kale, Y. Wang, S. Kandambeth, J. Czaban-Jozwiak, O. Shekhah, M. Eddaoudi, H. N. Alshareef, *J. Am. Chem. Soc.* **2021**, *143*, 19178.

[42] S. Li, M. Xia, C. Xiao, X. Zhang, H. Yu, L. Zhang, J. Shu, *Dalton Trans.* **2021**, *50*, 6520.

[43] J. N. Canongia Lopes, A. A. Padua, *J. Phys. Chem. B* **2006**, *110*, 3330.

[44] A. Mariani, R. Caminiti, M. Campetella, L. Gontrani, *Phys. Chem. Chem. Phys.* **2016**, *18*, 2297.

[45] H. K. Kashyap, J. J. Hettige, H. V. Annapureddy, C. J. Margulis, *Chem. Commun.* **2012**, *48*, 5103.

[46] C. Erinmwingbovo, M. S. Palagonia, D. Brogioli, F. La Mantia, *ChemPhysChem* **2017**, *18*, 917.

[47] J. Come, P.-L. Taberna, S. Hamelet, C. Masquelier, P. Simon, *J. Electrochem. Soc.* **2011**, *158*, A1090.

[48] A. J. Bard, L. R. Faulkner, *Electrochem. Methods* **2001**, *2*, 580.

[49] J. Moulder, W. Stickle, P. Sobol, K. Bomben, J. Chastain, *Handbook of X-ray Photoelectron Spectroscopy*, Vol. *40*, Perkin-Elmer Corporation, Eden Prairie, MN, USA **1992**, p. 221.

[50] M. C. Biesinger, L. W. Lau, A. R. Gerson, R. S. C. Smart, *Appl. Surf. Sci.* **2010**, *257*, 887.

[51] D. Jaeger, J. Patscheider, *J. Electron Spectrosc. Relat. Phenom.* **2012**, *185*, 523.

[52] M. A. Munoz-Marquez, M. Zarrabeitia, E. Castillo-Martinez, A. Eguia-Barrio, T. Rojo, M. Casas-Cabanas, *ACS Appl. Mater. Interfaces* **2015**, *7*, 7801.

**ADVANCED
SCIENCE NEWS**

www.advancedsciencenews.com

**ADVANCED
MATERIALS**

www.advmat.de

[53] A. Mullaliu, G. Aquilanti, L. Stievano, P. Conti, J. R. Plaisier, S. Cristol, M. Giorgetti, *J. Phys. Chem. C* **2019**, *123*, 8588.

[54] A. Mullaliu, G. Aquilanti, P. Conti, J. R. Plaisier, M. Fehse, L. Stievano, M. Giorgetti, *J. Phys. Chem. C* **2018**, *122*, 15868.

[55] X. Wu, J. J. Hong, W. Shin, L. Ma, T. Liu, X. Bi, Y. Yuan, Y. Qi, T. W. Surta, W. Huang, J. Neuefeind, T. Wu, P. A. Greaney, J. Lu, X. Ji, *Nat. Energy* **2019**, *4*, 123.

[56] G. Beamson, The Scienta ESCA 300 Database, **1992**.

[57] M. H. Lee, S. J. Kim, D. Chang, J. Kim, S. Moon, K. Oh, K.-Y. Park, W. M. Seong, H. Park, G. Kwon, B. Lee, K. Kang, *Mater. Today* **2019**, *29*, 26.

[58] L. Suo, D. Oh, Y. Lin, Z. Zhuo, O. Borodin, T. Gao, F. Wang, A. Kushima, Z. Wang, H. C. Kim, Y. Qi, W. Yang, F. Pan, J. Li, K. Xu, C. Wang, *J. Am. Chem. Soc.* **2017**, *139*, 18670.

[59] R. P. Vasquez, *Surf. Sci. Spectra* **1998**, *5*, 279.

[60] W. Deng, Y. Shen, J. Qian, Y. Cao, H. Yang, *ACS Appl. Mater. Interfaces* **2015**, *7*, 21095.

[61] D. A. Case, T. E. Cheatham, 3rd, T. Darden, H. Gohlke, R. Luo, K. M. Merz, Jr., A. Onufriev, C. Simmerling, B. Wang, R. J. Woods, *J. Comput. Chem.* **2005**, *26*, 1668.

[62] J. Wang, R. M. Wolf, J. W. Caldwell, P. A. Kollman, D. A. Case, *J. Comput. Chem.* **2004**, *25*, 1157.

[63] M. J. Frisch, G. W. Trucks, H. B. Schlegel, G. E. Scuseria, M. A. Robb, J. R. Cheeseman, G. Scalmani, V. Barone, G. A. Petersson, H. Nakatsuji, X. Li, M. Caricato, A. Marenich, J. Bloino, B. G. Janesko, R. Gomperts, B. Mennucci, H. P. Hratchian, J. V. Ortiz, A. F. Izmaylov, J. L. Sonnenberg, D. Williams-Young, F. Ding, F. Lipparini, F. Egidi, J. Goings, B. Peng, A. Petrone, T. Henderson, D. Ranasinghe, et al., *Gaussian09, Revision A.1*, Vol. *121*, Gaussian. Inc., Wallingford, CT, USA **2009**, p. 150.

[64] L. Martinez, R. Andrade, E. G. Birgin, J. M. Martinez, *J. Comput. Chem.* **2009**, *30*, 2157.

[65] M. Brehm, B. Kirchner, *J. Chem. Inf. Model.* **2011**, *51*, 2007.

[66] M. Brehm, M. Thomas, S. Gehrke, B. Kirchner, *J. Chem. Phys.* **2020**, *152*, 164105.

[67] B. H. Toby, R. B. Von Dreele, *J. Appl. Crystallogr.* **2013**, *46*, 544.

[68] D. O. Ojwang, J. Grins, D. Wardecki, M. Valvo, V. Renman, L. Häggström, T. Ericsson, T. Gustafsson, A. Mahmoud, R. P. Hermann, G. Svensson, *Inorg. Chem.* **2016**, *55*, 5924.

[69] A. Dent, G. Cibin, S. Ramos, A. Smith, S. Scott, L. Varandas, M. Pearson, N. Krumpa, C. Jones, P. Robbins, *J. Phys.: Conf. Ser.* **2009**, *190*, 012039.

[70] S. J. A. Figueroa, D. B. Beniz, J. C. Mauricio, J. R. Piton, S. A. Parry, G. Cibin, *J. Synchrotron Radiat.* **2018**, *25*, 953.

[71] B. Ravel, M. Newville, *J. Synchrotron Radiat.* **2005**, *12*, 537.